ACADEMIC PRESS

Available online at www.sciencedirect.com

SCIENCE DIRECT®

Journal of Computational Physics 185 (2003) 27–49

JOURNAL OF COMPUTATIONAL PHYSICS

www.elsevier.com/locate/jcp

Radial basis function interpolation in the quantum trajectory method: optimization of the multi-quadric shape parameter

Corey J. Trahan, Robert E. Wyatt *

Department of Chemistry and Biochemistry, Institute for Theoretical Chemistry, The University of Texas at Austin, Austin, TX 78712-1167, USA

Received 5 June 2002; received in revised form 20 October 2002; accepted 29 October 2002

Abstract

This paper investigates multi-quadric radial basis function (RBF) interpolation and its application in the quantum trajectory method (QTM) for wave packet propagation. In the multi-quadric, $\phi(r;\delta) = (r^2 + \delta^2)^{1/2}$, r is the radial distance from the observation point to the origin of the basis function, ϕ, and δ is known as the shape parameter due to its affect on the functional form of the basis function. The quality of any RBF interpolation scheme is dictated by the choice of this parameter. Many recent studies have investigated a suitable means for obtaining an "optimized" time-independent δ parameter. The purpose of this study, however, is to not only to find this "optimized" shape parameter, but also to analyze its time-dependence in four different dynamical models; the anisotropic harmonic oscillator, the downhill ramp, the uphill ramp, and a harmonic oscillator coupled with a downhill ramp. To obtain the optimized shape parameter at each time step, an algorithm similar to the leave-one-out method of cross-validation is utilized. The results for each of the four models are presented, and the feasibility and necessity of employing a shape parameter optimization algorithm for each of the models is discussed.

Keywords: Radial basis functions; Quantum trajectory method; Multi-quadric; Quantum hydrodynamics

1. Introduction

The de Broglie–Bohm casual hydrodynamic formulation of quantum mechanics was first introduced by Madelung [36] and de Broglie [6] in the late 1920s and then rediscovered by Bohm [3,4] in early 1950s. Today, a comprehensive study of the hydrodynamic formulation can be found in Bohm [5] and Holland's [23] books, both of which provide many of the technical details that are beyond the scope of this paper. In 1999, the quantum trajectory method (QTM) was introduced for the computational application of the de

* Corresponding author. Fax: 1-512-471-8696.
E-mail addresses: trahanc@mail.utexas.edu (C.J. Trahan), cman041@aurora.hpc.utexas.edu (R.E. Wyatt).

0021-9991/02/$ - see front matter
PII: S0021-9991(02)00046-3

Broglie–Bohm hydrodynamic formulation of quantum mechanics [59,60] and has since then attracted a large number of theoretical studies in quantum dynamics [1,2,7,24,25,31–35,44,56–60]. Such efforts have been focused on the QTM due to the low-resolution spatial grids needed to accurately capture wave packet dynamics, especially in multi-dimensional and unbound models. This asset of the QTM is a result of the Lagrangian framework inherent in the quantum hydrodynamic equations of motion. Because fluid elements are not fixed in space and are able to move along with the dynamics of the wave packet, the spatial domain needed for propagation is *much smaller* than in typical Eulerian fixed-grid simulations. Also, since the complex-valued quantum mechanical wavefunction is an oscillatory function in space, propagating the much smoother real-valued phase and amplitude functions requires *fewer grid points*, which can result in less computational work for obtaining spatial derivatives.

By far, the most challenging feature of the QTM, ironically, concerns the Lagrangian framework in which it flourishes. To integrate the equations of motion for reasonably long times, very accurate spatial derivatives are needed on an unstructured grid defined by the fluid element positions. This can become quite a difficult task, since errors tend to accumulate at boundaries or under-sampled regions with few grid points. The most widely used technique, so far, for obtaining function and derivative approximations has been the moving weighted least squares algorithm using a local polynomial basis. This method has been quite accurate for a limited number of models in the QTM (see Lopreore and Wyatt's publications on electronic transitions with quantum trajectories [33,34], Bittner's analysis of the double well potential [1], Wyatt and Na's analysis of multi-mode subsystem-bath dynamics [56], and Sales-Mayor et al.'s work on the molecular photodissociation [44]). Some problems can arise, however, with the use of polynomials that represent possible limitations to its application. According to Kansa [26], two drawbacks to polynomial schemes include polynomial snaking in higher-order models leading to poor derivative or integral estimates and the slow convergence of low-order polynomial approximations. Also, as the dimensionality of the model increases, the number of polynomial basis functions increases dramatically, significantly slowing down the solution of the linear system. Because of this, fitting schemes other than polynomial methods have been investigated for use with the unstructured mesh encountered in the Lagrangian frame. One such method includes radial basis function (RBF) interpolation.

There have been tremendous advances in RBF theory throughout the last decade in publications by Hardy [16–20], Madych [37–39], Carlson [9–11] and Foley [13], Schaback [45–53], and Kansa [26–30] to name only a few. In a study on the solution of the Lagrangian quantum fluid dynamical equations with RBF interpolation, Hu et al. [24,25] reported excellent results for free 2D and 3D wave packets, a 2D coherent state harmonic oscillator, and a 2D model for the photodissociation of NOCl. The first three of these four models were compared with the analytical solutions and the errors in the amplitude were found to be quite reasonable (see [24,25]). This particular study by Hu et al. utilized the power of the compactly supported multi-quadric (MQ) radial basis function for all derivative approximations. The multi-quadric has the form $\phi(r,\delta) = (r^2 + \delta^2)^{1/2}$, where r is the radial distance from the observation point to the origin of the basis function and δ is a free parameter determining the shape of the basis function. It is well known that the choice of this parameter can either greatly enhance or degrade the quality of the RBF interpolation scheme [54].

Recently, most interpolates found with radial basis functions, such as the multi-quadrics, contain a free parameter chosen such that the initial parameter value is used on all subsequent time steps. This parameter can be chosen through a "trial and error" optimization on the initial conditions of the system (i.e., find the best value of δ that minimizes a given error function for the initial amplitude and phase interpolations). In some cases, such as the models investigated by Hu, a *time-independent* δ parameter provides reasonable results. According to Carlson and Foley [11], however, the value of the optimal δ parameter strongly depends on the form of the function to be interpolated, and if this function changes with time, so should the shape parameter of the radial basis function.

It is the purpose of this study to investigate the optimization and time-dependence of the free parameter in the multi-quadric radial basis functions when they are employed in the quantum trajectory method. The parameter δ will be determined through utilization of an algorithm introduced by Rippa [43], which is similar to a cross-validation algorithm called the leave-one-out method. Since it is quite unreasonable to obtain an optimized shape parameter at each time step through brute force iteration, a simple means for updating δ is imperative. It is, therefore, our goal to emphasize the accuracy and simplicity of Rippa's $\delta(t)$ optimization algorithm for the purpose of implementing radial basis function interpolation in quantum trajectory calculations.

This study is organized as follows: Section 2 presents the quantum hydrodynamic equations of motion used in propagating the real-valued phase and amplitude functions. Section 3 provides some theoretical background on radial basis function interpolation and describes the algorithm that will be implemented for choosing the multi-quadric shape parameter at each time step. In Section 4, five time integrators are presented for solving the quantum equations motions and are compared in accuracy and time efficiency. In Section 5, three quantum mechanical models are described and the results of the QTM/RBF simulations with time-dependent multi-quadric shape parameters are given.

2. QTM methodology

To derive the quantum hydrodynamic equations of motion for a particle of mass, m, in an external potential $V(\vec{r},t)$, the polar form of complex-valued wave function, $\Psi(\vec{r},t) = R(\vec{r},t)\mathrm{e}^{\mathrm{i}S(\vec{r},t)/\hbar}$, is substituted into the time-dependent Schrödinger equation and separated into real and imaginary parts, resulting in the coupled pair of nonlinear partial differential equations

$$\frac{\partial S(\vec{r},t)}{\partial t} + \frac{(\vec{\nabla}S(\vec{r},t))^2}{2m} - \frac{\hbar^2}{2m}\frac{\nabla^2(\rho(\vec{r},t))^{1/2}}{(\rho(\vec{r},t))^{1/2}} + \mathrm{V}(\vec{r},t) = 0, \tag{1}$$

$$\frac{\partial \rho(\vec{r},t)}{\partial t} + \vec{\nabla}\cdot\left(\rho\frac{\vec{\nabla}S(\vec{r},t)}{m}\right) = 0, \tag{2}$$

where the probability density is defined as $\rho(\vec{r},t) = R(\vec{r},t)^2$. The first of the two equations is called the quantum Hamilton–Jacobi equation and is identical in form to its classical counterpart except for the addition of the purely quantum term

$$Q(\rho,\vec{r},t) = -\frac{\hbar^2}{2m}\frac{\nabla^2(\rho(\vec{r},t))^{1/2}}{(\rho(\vec{r},t))^{1/2}}. \tag{3}$$

David Bohm has named this term the quantum potential [3,4]. The quantum potential is the source of all quantum effects, and in the limit that $Q \to 0$, the classical Hamilton–Jacobi equation is recovered. An important feature of Q is that it depends only on the curvature of the wavefunction amplitude, not on its magnitude.

Eqs. (1)–(3) have been derived analytically from the Schrödinger equation; however, to numerically integrate these equations the initial wave packet must be broken down into np discrete fluid elements with positions $\vec{r}_i$. Each fluid element can be conceived as pursuing a definite continuous track in space and time according to a guidance equation

$$\dot{\vec{r}} = \vec{v} = \frac{1}{m}\vec{\nabla}S(\vec{r},t). \tag{4}$$

Along a trajectory, the density and phase of each fluid element is obtained by integrating Eqs. (1) and (2), while the fluid element velocities and positions are found by the evaluation and integration of Eq. (4). To do this, the initial conditions $\vec{r}(0)$, $\vec{v}(0)$, and $\rho(0)$ must be specified. An important feature of the QTM is that upon discretization, Eq. (4) provides a description of an ensemble of *coupled* trajectories, each with different fluid element initial conditions. These trajectories are coupled by the *nonlocal* quantum potential from Eq. (3).

If the gradient of the quantum Hamilton–Jacobi equation is taken, and the Lagrangian total time derivative, $\mathrm{d}/\mathrm{d}t = \partial/\partial t + \vec{v}\cdot\vec{\nabla}$, is substituted into Eqs. (1) and (2), the quantum equations of motion can be derived in their more familiar forms

$$m\dot{\vec{v}} = -\vec{\nabla}(V(\vec{r},t) + Q(\rho,\vec{r},t)), \tag{5}$$

$$\frac{\mathrm{d}\rho(\vec{r},t)}{\mathrm{d}t} = -(\vec{\nabla}\cdot\vec{v})\rho, \tag{6}$$

where the first equation is similar to the Newtonian classical law of motion and the second is the probability continuity equation. The continuity equation, can be analytically integrated giving

$$\rho(\vec{r},t+\mathrm{d}t) = \mathrm{e}^{-\int(\vec{\nabla}\cdot\vec{v})\,\mathrm{d}t}\rho(\vec{r},t), \tag{7}$$

where the exponential operator is called the density propagator. In this operator, the integral is evaluated along the trajectory traversed by the fluid element in time.

As stated before, one very important computational benefit of the QTM is in the spatial discretization of the phase and amplitude instead of the wave function directly. Very high-resolution spatial grids are frequently needed in fixed-grid Eulerian methods due to the oscillatory nature of the complex-valued wavefunction, especially during high-energy simulations and models with many degrees of freedom. However, because the phase and amplitude remain relatively smooth in time, propagating Eqs. (4)–(6) requires fewer grid points for function approximation. In the past, to further alleviate the difficulty of obtaining accurate derivatives for substitution into the equations of motion, $C = \ln(R)$ has been propagated instead of the amplitude directly. This replacement can be beneficial for two reasons. First, C will, in general, be smoother than R, since it is not an oscillating function in space. For example, the typical Gaussian wave packet reduces to a quadratic polynomial if the logarithm is taken. Secondly, the range of C may be much smaller than R. For example, if R ranges from $10^{-7} \leqslant R \leqslant 1$, the range for the C is only $-16 \leqslant R \leqslant 0$. Using this replacement, the quantum potential to be substituted into the quantum Hamilton–Jacobi is derived from Eq. (3) to be

$$Q = -\frac{\hbar^2}{2m}\{\nabla^2 C + \vec{\nabla}C\cdot\vec{\nabla}C\}. \tag{8}$$

The C amplitude was propagated in all three of the models studied and the quantum potential was found according to the above equation.

3. Spatial discretization

3.1. RBF interpolation

To solve Eqs. (4)–(6) computationally, the continuous probability distribution is discretized into np fluid elements at $t = 0$. Each fluid element has a mass m, an initial value location, $\vec{r}_i(t=0)$, and is identified by a descriptor, $D_i(t) = \{\vec{r}_i, \vec{v}_i, \rho_i, S_i\}$, which stores the state of the ith fluid element at future times. At each time

step, extremely accurate spatial derivatives (i.e., $\vec{\nabla}S, \nabla^2 R$, etc.) are needed at these locations for substitution into the equations of motion before time discretization and wave packet propagation can proceed. Obtaining these spatial derivatives efficiently and accurately on the unstructured mesh encountered in the Lagrangian frame of reference represents the greatest challenge for applications of the QTM.

In the last decade or so, radial basis function interpolation has attracted considerable interest due to its simplicity in application and its potential to interpolate multi-variate scattered data relatively accurately [8–11,13–22,24–30,37–41,43,45–55,61,62]. The typical interpolation scenario in the QTM involves approximating the phase or amplitude with known descriptor values, $\{f(\vec{r}_i),\ i = 1, 2, \ldots, np\}$ at each of the discrete fluid element locations, $\{\{x_i^1, x_i^2, \ldots, x_i^d\},\ i = 1, 2, \ldots, np\} \in R^d$ for a d-dimensional system, such that

$$F(\vec{r}_i) = f_i, \tag{9}$$

where $F(\vec{r}_i)$ is the interpolate of f, the descriptor value at the ith fluid element. The RBF interpolate of the function f has the form

$$F(\vec{r}_i) = \sum_{j=1}^{np} a_j \phi(\|\vec{r}_i - \vec{r}_j\|), \tag{10}$$

where $\|\cdot\|$ denotes the Euclidean norm, and $\phi(\|\vec{r}_i - \vec{r}_j\|)$ are the radial basis functions.

The coefficients of Eq. (10), $\vec{a}$, are found by solving the linear system

$$\underline{\underline{\Phi}}\vec{a} = \vec{f}, \tag{11}$$

where $\underline{\underline{\Phi}}$ is a collocation matrix with elements $\phi_{ij} = \phi(\|\vec{r}_i - \vec{r}_j\|)$. A few examples of the some well-known RBFs are

$$\begin{aligned}
&\phi(r) = (-1)^m(\delta^2 + r^2)^{\beta/2} \quad (2m - 2 < \beta < 2m), && \text{multi-quadrics,}\\
&\phi(r) = (\delta^2 + r^2)^{-\beta/2} \quad (\beta > 0), && \text{inverse multi-quadrics,}\\
&\phi(r) = (-1)^m r^{2m-2}\ln(r), && \text{thinplate splines,}\\
&\phi(r) = (-1)^m(\delta^2 + r^2)^{m-1}\ln(\delta^2 + r^2)^{1/2}, && \text{shifted thin-plate splines,}\\
&\phi(r) = \mathrm{e}^{-(\delta r)^2}, && \text{Gaussians.}
\end{aligned} \tag{12}$$

One of the most popular radial basis functions is the multi-quadric (MQ) developed by Hardy [20]. Micchelli's [40] has proved that the multi-quadric is always solvable for distinct data, and that the MQ coefficient matrix of rank np has one positive real eigenvalue and $(np - 1)$ negative real eigenvalues. The multi-quadric with $\beta = 1$ is the most widely used and has the form

$$\phi(\|\vec{r}_i - \vec{r}_j\|) = (r_{ij}^2 + \delta^2)^{1/2}, \tag{13}$$

where

$$r_{ij} = \left(\sum_{k=1}^{d}(x_i^k - x_j^k)^2\right)^{1/2}, \tag{14}$$

and where, for the purposes of this study, δ is a parameter that is independent of the basis function. Because the multi-quadrics have exponential convergence properties [39] and have been ranked the best in accuracy of all RBFs according to Franke's review paper [14], it was the RBF chosen for the models discussed in Section 5.

3.2. Optimization of RBF parameter

3.2.1. Background of RBF parameter optimization

It is well known that the choice of the parameter in Eq. (13) has a large influence on the interpolation ability of the RBF basis [54]. To examine how the δ parameter affects the shape of the multi-quadric basis function, the limit of the function can be taken as $\delta \to \infty$ and $\delta \to 0$. From Fig. 1 it can seen that as δ increases, so does the relative smoothness of the basis function, however, at relatively large values of δ, the function becomes linear near the center and begins to "wash out" the coordinate dependence of the basis function. This can lead to difficulties when trying to obtain distinct entries in the coefficient matrix for better conditioning. On the other hand, as $\delta \to 0$ the multi-quadric begins to have the shape of a cone with a cusp or discontinuous derivative at the center. It is, therefore, easy to visualize why extremely small shape parameters do not give very smooth interpolates and are generally not preferred. Understanding these features and how they relate in the collocation-like scheme of RBF interpolation is vital when considering optimization of the free parameter RBFs. Tarwater [54] has shown that the RMS errors of the interpolates decrease with increasing δ until an optimum value is obtained, and that beyond this optimum value the collocation matrix becomes extremely ill-conditioned, resulting in increasing errors. This optimum shape parameter thus represents the best compromise between the smoothness of the interpolate and the conditioning of the coefficient matrix. Obtaining δ_{opt} continues to be an active area of investigation in RBF interpolation, and many papers have been written on circumventing the ill-conditioning of the coefficient matrix to assuage this task (see [30]). A few of the proposed methods for determining good shape parameters include the following: Hardy's use of the equation $\delta = 0.815d$, where d is the average distance between the ith data point and its nearest neighbor [20], Foley's scheme for selecting δ by minimizing the average root-mean-square (RMS) difference between the multi-quadric and inverse multi-quadric [13],

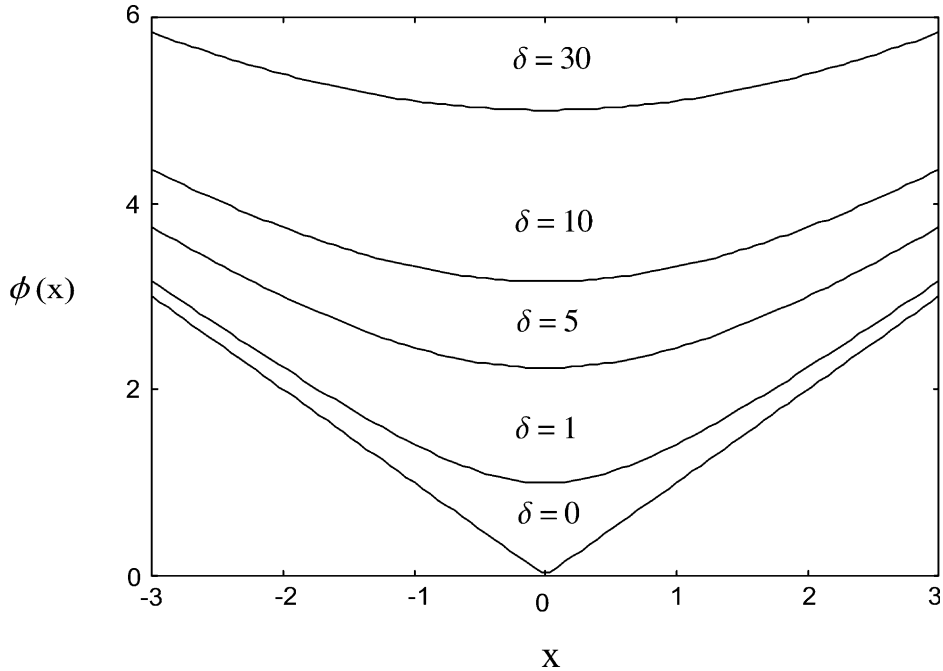

Fig. 1. The multi-quadric radial basis function for five different δ parameters. An important feature of this figure is the cusp that forms as the parameter approaches zero, resulting in a discontinuous derivative at the origin of the basis function.

Kansa and Carlson's method of selecting local shape parameters (shape parameters that are basis function-dependent) [29], and lastly, Rippa's method of "cost" minimization [43], which is similar to Goldberg's method of cross-validation [15]. It is the purpose of this paper to investigate further, from the QTM perspective, Rippa's algorithm for shape parameter optimization through Cost functional minimization.

3.2.2. The cross-validation method

To optimize the multi-quadric shape parameter, a method for estimating the prediction error of each trial δ must be found. One way of doing this is to first portion the data set into N partitions, which may or may not be of equal size. Using the $N-1$ partitions as a new data set, often called the "learning set", an error can be calculated against the remaining data partition called the "validation set". For each of the N validation sets there is a corresponding error found by fitting its particular learning set. Each of the N error terms can then be averaged to give the prediction error of the complete data set for a particular parameter value. Such "resampling" methods make no assumptions on the statistics of the data or on the type of model function being estimated. The above technique is known as *cross-validation* and is widely used for parameter optimization problems [12,21]. Rippa's algorithm for multi-quadric parameter optimization can be compared to a form of cross-validation known as the "leave-one-out" method. This particular form of cross-validation is especially suitable for relatively small data sets, since large partitioning of an already under-sampled data set can lead to misrepresentation of the function to be approximated. In the leave-one-out method, one data point is used for error estimation and all other $np-1$ data points are used as a new data set. The prediction error for a particular parameter can then be calculated by averaging the np error terms.

3.2.3. Rippa's algorithm

In Rippa's algorithm for choosing δ, a "Cost functional" is minimized that imitates the behavior of the RMS error between the interpolate and the unknown function from which the data vector, $\vec{f}$, was sampled [43]. The Cost functional is defined as the L_1 norm of an error vector,

$$\mathrm{Cost}(\delta) = \sum_{k=1}^{np} |E_k|, \tag{15}$$

with error vector elements

$$E_k = f_k - S^{(k)}(\vec{r}_k), \quad k = 1, 2, \ldots, np, \tag{16}$$

where f_k is the function value at the kth data point, and

$$S^{(k)}(\vec{r}_k) = \sum_{j=1, j\neq k}^{np} a_j^{(k)} \phi(\|\vec{r}_k - \vec{r}_j\|) \tag{17}$$

is the interpolate of the function f found *without* using the data point $\vec{r}_k$ as a center. The learning set for a particular E_k can then be defined as all data values other than f_k, which is the validation point in the leave-one-out form of cross-validation.

Normally, the computational work of one evaluation of the Cost functional would require a LU decomposition of the $(np-1)\times(np-1)$-order linear system in addition to calculating all np error terms in the vector $\vec{E}$. However, Rippa's derivation includes a method of obtaining $\vec{E}$ requiring only one LU decomposition of the original system of equations

$$\underline{\underline{\Phi}}\vec{a} = \vec{f}, \tag{18}$$

plus the cost of N solutions to a new linear system

$$\underline{\underline{\Phi}}\vec{m}^{(k)} = e^{(k)}, \tag{19}$$

where $e^{(k)}$ is the kth column of the $np \times np$ identity matrix. Using Eqs. (16)–(19), an error vector can be derived such that

$$E_k = f_k - S^{(k)}(\vec{r}_k) = \frac{a_k}{m_k^{(k)}}, \tag{20}$$

where a_k and $m_k^{(k)}$ are the kth coefficients of the two system of equations (for the full derivation, see [43]). Utilizing the above equation gives $O(np^3)$ operations for the evaluation of one Cost function, the same order as the original LU decomposition of $\underline{\underline{\Phi}}$.

The effect of minimizing the Cost functional on a 2D normalized Gaussian function can be seen in Fig. 2, plots (a) and (b). The graph of the Cost is similar in form, though not identical, to the graph of the RMS error calculated from the test Gaussian. The most important feature of the two figures is the value of $\delta_{\text{good}}^{\text{Cost}}$ in comparison to $\delta_{\text{opt}}^{\text{RMS}}$ found at an approximately quadratic minimum before numerical breakdown occurs when $\delta \geqslant 0.75$. A significant result of the similarity between the two results is that by minimizing the Cost as a function of δ and finding $\delta_{\text{good}}^{\text{Cost}}$, one can simultaneously approximate $\delta_{\text{opt}}^{\text{RMS}}$. In his paper on Cost functional minimization, Rippa reports excellent correlation of the two minima, and his results for RBF/MQ interpolation on several of Franke's test functions were extremely accurate.

The only unfortunate feature of the leave-one-out algorithm is that an iterative procedure over the shape parameter is required to obtain an approximate minimum to the Cost function. To reduce the number of iterations needed, subroutines *mnbrak* and *brent* from Numerical Recipes [42] were used for the minimization procedure. On input, two initial shape parameters of $\delta = 0.1$ and 0.2 were used for bracketing the minimum, and a tolerance of 0.01 was assigned for the convergence test in Brent's method. The number of iterations required to converge on a minimum were, on average, 9.5 for each interpolation. Because this number was relatively small, utilization of Rippa's algorithm at *each time step* to determine a time-dependent shape parameter was feasible, though this iterative procedure was the rate-determining step in all of the QTM/RBF models in Section 5.

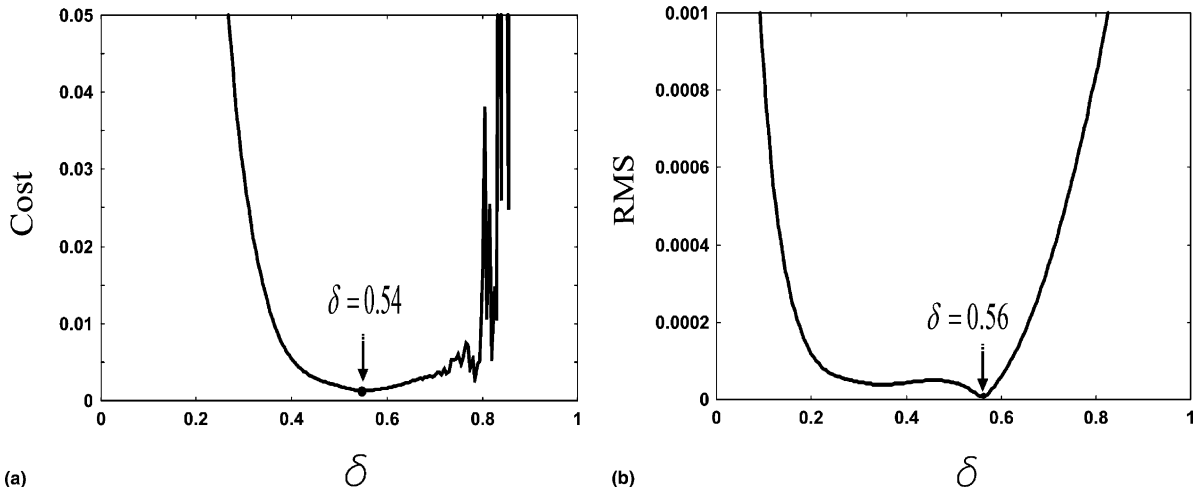

Fig. 2. Plots (a) and (b) illustrate the form of the Cost function and the average RMS error of a 2D normalized Gaussian test function, $f(x,y) = N\exp^{-25((x-.5)^2+(y-.5)^2)}$. The optimum RMS obtained from iteration was 7.96×10^{-6}, corresponding to a δ parameter of 0.56. The value of the Cost minimization algorithm was 0.54, relatively close to the optimum value.

4. Time discretization and propagation

After spatial discretization, Eqs. (4)–(6) become a set of ordinary differential equations in time and can be numerically integrated quite easily. Five numerical integrators were studied and compared to test their accuracy and time efficiency. To examine the accuracy of each integrator, a 2D free Gaussian wave packet of the form (at $t = 0$)

$$\Psi(x,y,t) = \sqrt{\frac{2\sqrt{\beta_x\beta_y}}{\pi}}\mathrm{e}^{-\beta_x(x-x_0)^2-\beta_y(y-y_0)^2} \tag{21}$$

was propagated in time by integrating the Lagrangian equations of motion, and the exact amplitude at each time was calculated for comparison according to the analytical time-dependent solution. As stated before, instead of propagating $R(x,y,t)$ directly, $C(x,y,t)$ was used to ensure exact quadratic polynomial fits and to eliminate any spatial errors within machine precision. The analytical form for the time dependence of C for a free 2D wave packet can be written as

$$C(x,y,t) = -\frac{1}{2}\left\{\frac{1}{2}\ln(\pi\sigma_x) + \frac{1}{2}\ln(\pi\sigma_y) + \frac{1}{\sigma_x}(x - x_0 - v_{x0}t)^2 + \frac{1}{\sigma_y}(y - y_0 - v_{y0}t)^2\right\} \tag{22}$$

with

$$\sigma_x = \frac{1}{2\beta_x} + \frac{2\beta_x t^2}{m}, \quad \sigma_y = \frac{1}{2\beta_y} + \frac{2\beta_y t^2}{m}, \tag{23}$$

where m, v_{x0}, v_{y0}, x_0, and y_0 are the mass, initial velocities, and initial positions of the fluid elements. Table 1 lists the parameters of the initial wave packet.

The accuracy of five time integrators are compared in Table 2. Average errors were calculated according to the equation

$$\text{error} = \frac{1}{np}\sum_{i=1}^{np}\left|\mathrm{e}^{C(x,y,t)^{\text{exact}}} - \mathrm{e}^{C(x,y,t)^{\text{calculated}}}\right|. \tag{24}$$

Also, all methods described as being implicit in Table 2 are only implicit in the amplitude update. The new phase, position, and velocities are obtained explicitly by the integrator labeled before the forward slash. The

Table 1
Free 2D wave packet parameters

β_x	8[a]
β_y	8
Energy	4500 cm^{-1}
m (mass)	2000
(x_0, y_0) (initial wave packet center)	(0,0)
v_{x0} (all fluid elements given same initial x-velocity)	0.0045
v_{y0} (all fluid elements given same initial y-velocity)	0
Δx (initial fluid element separation in x)	0.12
Δy (initial fluid element separation in y)	0.12
np (the total number of fluid elements)	11×11 grid, $np = 121$
dt (time step)	1.0

[a] All units are atomic (a.u.) unless otherwise given.

Table 2
Comparison of the accuracy of five time integrators for a 2D free wave packet

Integration scheme	Error[a]
Euler/trapezoid[b]	1.0078×10^{-4}
Leap frog (multi-step)[c]	2.6352×10^{-7}
Fourth-order Adam's-Bashforth (multi-step)	1.9777×10^{-10}
Fourth-order Adam's-Bashforth/Adam's-Moulton (multi-step)[b]	1.5274×10^{-10}
Fourth-order Runge–Kutta	1.7718×10^{-12}

[a] Errors are taken after 2500 time steps.
[b] These time integrators use implicit routines for amplitude update.
[c] Multi-step integrators initiated with analytical solution for a free 2D wave packet.

amplitude can be updated implicitly by evaluating the $\vec{\nabla} \cdot \vec{v}$ in the exponential of Eq. (7) with the new velocities calculated from the previously updated phase.

The semi-implicit Euler/trapezoid method was very time efficient but the least accurate, having a truncation error of $O(dt)$. Because initiating steps or intermediate steps are not needed, the Euler/trapezoid code can be executed as fast as the spatial discretization and derivative evaluations will allow. Unfortunately, very small time steps are needed as the phase and amplitude become less smooth in time. By decreasing the time step, the time efficiency of the Euler/trapezoid method is compromised to the point where it is no longer a viable integration technique. Such was the motivation for studying higher-order numerical integration methods.

Another commonly used method of integration is the "leap frog" technique [42]. It is but one of the many multi-step methods utilizing information from previous time steps to advance the solution to new times. Other examples of multi-step methods include the Adam's-Bashforth and Adam's-Moulton algorithms. Such methods are particularly attractive since a predetermined order of accuracy can be obtained by increasing the number of prior time steps used in the extrapolation. The difficulty in the multi-step methods, however, is initiating the integrator. Depending on the order of accuracy needed, a given number of steps must be initiated with the same order of accuracy by either a highly accurate one-step method, or by taking many smaller Euler steps within the given time step. In the results of Table 2, the analytical time-dependent expressions for the phase and amplitude are used to propagate the wave packet to obtain the initial time steps needed for extrapolation. According to the results obtained, the increased accuracy of the "leap frog" two-step routine over the Euler/trapezoid method is approximately three orders of magnitude. The increased accuracy is primarily due to the two-step method having a truncation error of $O(dt^2)$ instead of $O(dt)$. On moving from the two-step "leap frog" method to the four-step Adam's-Bashforth/Adam's-Moulton method, the accuracy was increased by approximately six orders of magnitude from the Euler/trapezoid method, a very dramatic improvement due to the new truncation error of $O(dt^4)$. It should be emphasized that apart from initiating the above multi-step algorithms, each requires about the same propagation time as an Euler/trapezoid simulation.

The last numerical integration method studied was the fourth-order Runge–Kutta (RK4) algorithm. Although RK4 is the least time efficient of the five methods studied, requiring four spatial derivative evaluations for every interpolation at each time step, it is a one-step procedure and does not need to be initiated. More importantly, RK4 is known for its robust ability to obtain accurate results for differential equations with smooth to relatively "rough" or stiff solutions [42]. As can be seen from the table, RK4 produced highly accurate solutions for the free 2D wave packet. Although the results obtained from RK4 were the best of all the algorithms tried, it was not used as the primary time integrator since evaluating four spatial derivative at each time step becomes very time consuming when coupled with the RBF shape parameter optimization.

For the models discussed in this paper, the Adam's-Bashforth/Adam's-Moulton fourth-order semi-implicit method was used as the time integrator. To initiate the multi-step algorithm, RK4 was used for the first four time steps. This particular combination proved to be the best choice for relatively fast and accurate solutions. It should be stated here that although a high-order time integrator was used, the amplitude and phase are relatively smooth functions in time, and most of the difficulties with the QTM are not in choosing the time-integrator or an appropriate time step, but in obtaining spatial derivatives needed for substitution into the hydrodynamic equations of motion.

5. Models

5.1. Model 1: the anisotropic harmonic oscillator

To test the RBF/MQ interpolation algorithm using Cost functional minimization, a 2D anisotropic harmonic oscillator potential of the form

$$V(x,y) = k_1x^2 + k_2y^2, \tag{25}$$

with force constants $k_1 = 0.009$ and $k_2 = 0.036$, was used. To obtain periodic motion of the type executed by a classical oscillator, a wave packet must be used and the TDSE utilized for its time evolution. Table 3 lists the parameters of the propagated Gaussian wave packet.

The results of the time propagation can be seen in Fig. 3, plots (a)–(c). In plots (a) and (b), two cross-sections are shown emphasizing the anisotropic symmetry of the harmonic well. Upon comparison, the x-trajectories of the y cross-section have larger amplitudes and a longer period than the y-trajectories of the x cross-section. This was expected since $k_2 > k_1$. Computational break down occurred after four x-periods and eight y-periods of the oscillator (about 150 fs or 6100 time steps into the computation). Until this break down occurred, the results are what were expected for the anisotropic oscillator. For example, in this particular potential, a classical particle initiated at the center of the wavepacket follows a lissajous figure. In the quantum simulation, the fluid element positioned at the center of initial quantum wave packet, where there is no quantum potential, followed the same trajectory.

In Fig. 3, plot (c), the time-dependence of the multi-quadric shape parameter, is displayed for the amplitude interpolation over the period of evolution of the wave packet. At this point, it should be emphasized that since the wave packet amplitude remains Gaussian in form throughout the entire computation, the log of the amplitude is quadratic and can be easily reproduced from very few fluid elements using polynomial

Table 3
2D wave packet parameters for the anisotropic harmonic oscillator

β_x	8
β_y	8
Energy	8000 cm^{-1}
m	2000
(x_0, y_0)	(0,0)
v_{x0}	0.014
v_{y0}	0.023
Δx	0.12, 0.075
Δy	0.12, 0.075
np	11×11 grid, $np = 121$
	17×17 grid, $np = 289$
dt	1.0

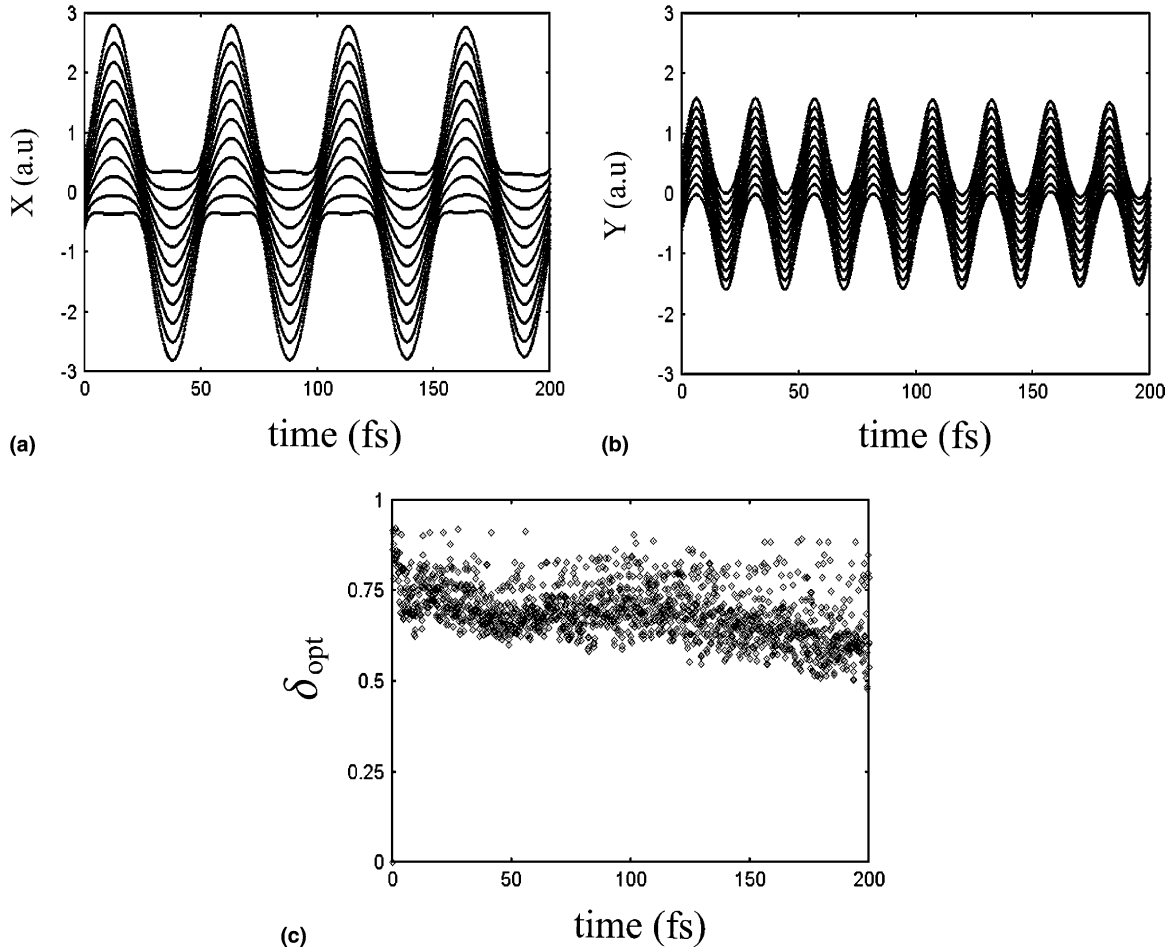

Fig. 3. Plot (a) displays the x-coordinates of the quantum trajectories at the $y = 0$ cross-section for the anisotropic harmonic oscillator potential described in model 1. Plot (b) shows the y-coordinates of the trajectories at the $x = 0$ cross-section. Plot (c) displays the time-dependence of the shape parameter on the 11×11 grid.

least squares or interpolation schemes. However, because the purpose of the simulation was to test the RBF/MQ scheme with a simple classical potential and obtain a description of the time-dependence of the MQ shape parameter, this particular model was quite beneficial to the analysis. An important feature of plot (c) is the initial average decay of the optimized shape parameter. This particular feature will be seen in each of the three models discussed. One explanation of the decay is that, initially, the grid is structured and each of the fluid elements positions are computationally distinct from one another (by computationally distinct, it is meant that the rows/columns of the RBF collocation matrix to be solved are computationally more independent than in an unstructured grid, where fluid elements may be positioned very close together leading to similar entries into the collocation matrix). As the rows and columns become more independent the coefficient matrix becomes better conditioned, allowing for larger shape parameters. In time, as the grid becomes unstructured, fluid elements may be "squeezed" together by the external potential, resulting in small separations in their positions. In such a scenario, the rows/columns become more dependent, and the coefficient matrix becomes ill-conditioned, giving rise to smaller shape parameters from the optimization

algorithm. In the anisotropic oscillator model, the fluid elements were squeezed together as the wave packet reflected off the edges of the potential well.

A second important feature of Fig. 3, plot (c), is that the optimized shape parameters chosen throughout the wave packet propagation were mostly scattered between $0.60 \leqslant \delta \leqslant 0.80$. This large fluctuation in the shape parameter was found when the initial grid was relatively coarse, such as the 11×11 grid used in this model. In a second isotropic harmonic oscillator model studied, a finer 17×17 grid was used. On this grid, there was less fluctuation about the average, as most of the optimized shape parameters were in the range of $0.40 \leqslant \delta \leqslant 0.50$ (see Fig. 4). It is also important to notice that for higher resolution grids, such as the 17×17 case where there are more fluid elements with smaller separations, smaller shape parameters are chosen by the optimization algorithm.

The spreading of the δ parameter for coarse grids, such as the 11×11 example, provides an explanation for the success of the *time-independent* shape parameters used in past RBF/QTM models, since most constant parameters within this range will, in general, be suitable for multi-quadric interpolation. Also, because of the notoriously ill-conditioned RBF coefficient matrix, studies, such as those by Hu [24,25], are limited to few grid points with relatively large initial fluid element separation. While coarse grids are all that is needed for amplitudes that remain Gaussian/quadratic in time, such as the free particle and harmonic oscillator, greater resolution is needed for more interesting problems that may include scattering from barriers and interference effects. As the grid resolution increases, the fluctuation range of the optimized shape parameters becomes smaller, and while this may not be a problem for models with a relatively constant optimal δ parameter, it may present problems if a time-dependent shape parameter is needed, such as in model 3.

Lastly, it should be emphasized that though a constant δ is all that is needed for some simple models such as the free Gaussian wave packet or the propagation of a Gaussian wave packet in a harmonic potential, Rippa's optimization algorithm can be very beneficial for initiating the wave packet propagation. For example, instead of iterating over a large number of parameters to obtain one suitable for use in the simulation, the parameter can be chosen automatically by the optimization algorithm.

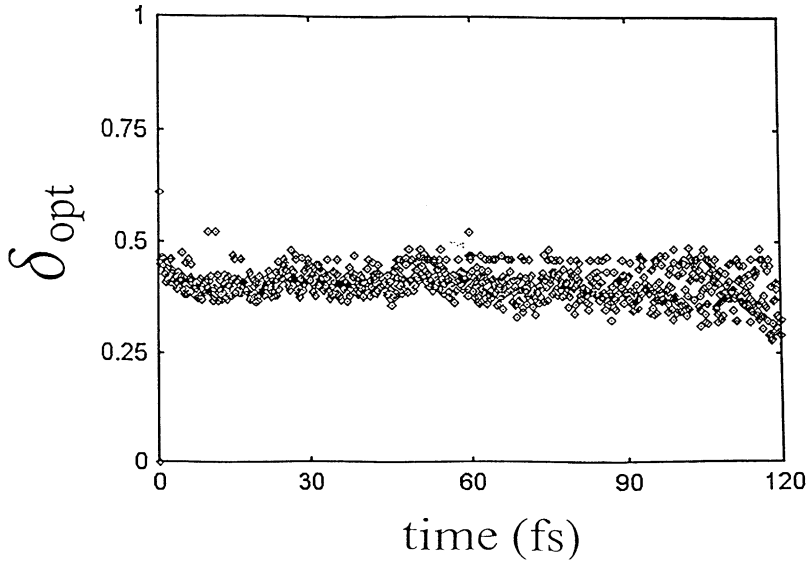

Fig. 4. The time-dependence of the shape parameter for the anisotropic harmonic oscillator potential of model 1 using a 17×17 grid.

5.2. Model 2: the downhill and uphill ramp

5.2.1. The downhill ramp

The second model studied was the evolution of an initial 2D Gaussian wave packet on a downhill ramp potential energy surface of the form

$$V(x) = \frac{V_0}{1 + e^{-2.5(x-1)}}, \tag{26}$$

with $V_0 = -1500$ cm^{-1}. This particular model is important for understanding exothermic reaction kinetics and photodissociation on excited state potential energy surfaces. Of course, since the external potential is independent of the y-coordinate, the Schrödinger time-dependent wave equation can be separated and solved as two independent 1D problems. However, because the purpose of this study was to gain insight into how the optimum multi-quadric shape parameter changes in a time-dependent simulation, and knowing that the 2D coefficient matrix plays a vital role when finding this parameter, the simulation was carried out as a 2D study. A similar 1D quantum trajectory analysis on the downhill ramp potential can be referenced in Lopreore and Wyatt's study [31].

The initial wave packet parameters for the downhill ramp model are listed in Table 4. Four different simulations were studied with initial wave packet energies of 0, 500, 1500, and 8000 cm^{-1}, respectively. The transmission probabilities, found by numerically integrating the probability density of all fluid elements with locations $x_i > 2.2$, are shown in Fig. 5, plot (a). Convergence on a transmission probability was obtained for the two higher energy wave packets, however, as can be seen from the plot, the wave packets with initial energies of 0 and 500 cm^{-1} did not converge completely, though the simulations proceeded to extremely large times (over 15,000 time steps) without breakdown. Incorrect transmission probabilities at large times were expected, however, since relatively few fluid elements were used initially, and these fluid elements were scattered at large distances asymmetrically as time progressed. The result of the low resolution was a breakdown of the trapezoid method used for numerical integration. Because of this, only the first 70 fs (approximately 5800 time steps) are displayed in plots (a)–(c).

Plot (b) of Fig. 5 shows x trajectories at the $y = 0$ cross-section for the 1500 cm^{-1} initial energy wave packet. One important feature of this plot is the reflection of the first three fluid elements to the $-x$ direction. Classically, there is no turning point, and all the fluid elements will proceed down the potential ramp while increasing velocity. However, it is well known that in the quantum case, wave packet reflection can occur, resulting in only partial transmission of the total probability.

Lastly, in Fig. 5, plot (c), the δ parameter for the amplitude interpolation was plotted vs. time for the wave packet with energy 1500 cm^{-1}. Other than the previously discussed initial exponential decay, there

Table 4
2D wave packet parameters for the downhill ramp

β_x	8
β_y	8
Energy	$0, 500, 1500, 8000$ cm^{-1}
m	2000
(x_0, y_0)	(0,0)
v_{x0}	0, 0.0023, 0.0068, 0.0365
v_{y0}	0
Δx	0.075
Δy	0.075
np	17×17 grid, $np = 289$
dt	0.5

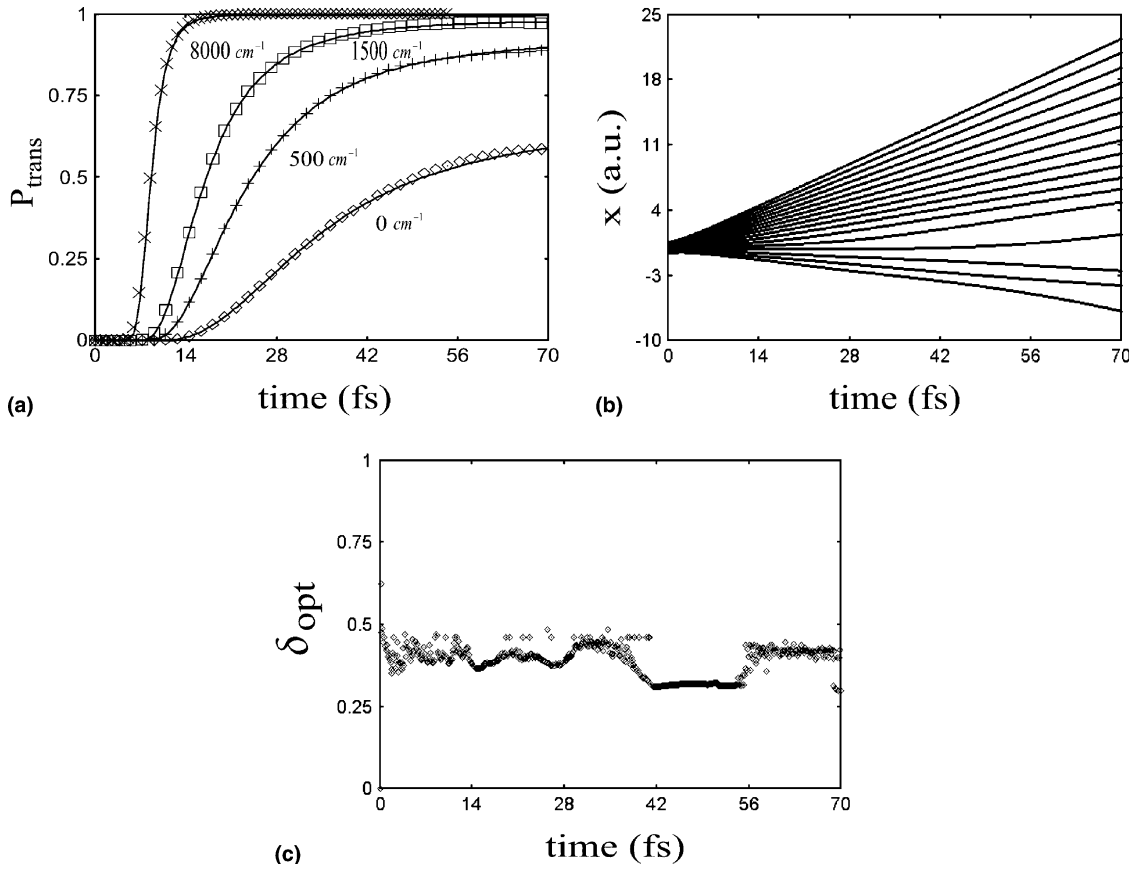

Fig. 5. Plot (a) displays the QTM/RBF results for the transmission probability as a function of time for four wave packets of different energies traveling on a downhill potential. The solid line was calculated from a finite difference, fixed-grid method. Plot (b) shows x trajectories at the $y = 0$ cross-section for the wave packet with energy of 1500 cm^{-1}. Plot (c) displays the optimized shape parameter in time for the same energy wave packet.

seems to be no general trend in the parameters chosen for each of the simulations. One thing to notice, however, is the inexplicable growing oscillation that occurs in time. Since there is no oscillation of the amplitude in any of the above simulations, this particular feature must be related to the numerical algorithms used in the δ parameter optimization or the QTM driver code.

Each of the four simulations for model 2 was also studied with a *constant* multi-quadric shape parameter of 0.4. Because of the extremely small reflection probability for the wave packet energies studied, there was no difficulty in the time propagation of the wave packets for this parameter, and comparable results to that of the time-dependent parameter simulations were obtained.

5.2.2. The uphill ramp

In this study, five wave packets of different energies were propagated using the same potential as the downhill ramp, Eq. (26), only with $V_0 = +1500$ cm^{-1}. Table 5 displays the initial conditions used for this model. Propagation of a wave packet into an uphill ramp presents a slightly more complicated model than that of the downhill potential since more bifurcation can occur resulting in large interference effects in the reflected part of the wave packet. Ideally, a finer grid resolution than 17×17 is needed to capture all of the

features of the solution in time (such as the "ripples" in the reflected packet); however, accurate transmission probabilities can still be obtained without high resolution, as can be seen from the results in Fig. 6, plot (a). The wave packets on the uphill potential, however, did not propagate as far as those on the downhill potential, and the QTM algorithm broke down soon after 50 fs (4100 time steps).

In Fig. 6, plot (b), the time-dependence of the multi-quadric shape parameter is shown. The results show a relatively constant optimal parameter until about 32 fs, at which the average parameter value begins to decay until computational break down. This decay was a typical "forecasting" of the break down of the QTM/RBF algorithm, most likely occurring from *growing interpolation errors* in regions of few grid points and large solution gradients or curvatures. It should be emphasized that these errors were due to the low-resolution grids used in the interpolation algorithm and not the inherent nature of the solution in the models discussed. Another likely explanation of the QTM/RBF algorithm break down is that as time progresses, trajectories can approach one another and grid points separations can be very small. As stated before, such is a rather unfortunate feature of Lagrangian schemes, and the affect is further aggravated by the conditioning of the RBF coefficient matrix.

Table 5
2D wave packet parameters for the uphill ramp

β_x	8
β_y	8
Energy	500, 1500, 3000, 4500, 6000 cm^{-1}
m	2000
(x_0, y_0)	(0,0)
v_{x0}	0.0022, 0.0068, 0.0137, 0.0205, 0.0273
v_{y0}	0
Δx	0.075
Δy	0.075
np	17×17 grid, $np = 289$
dt	0.5

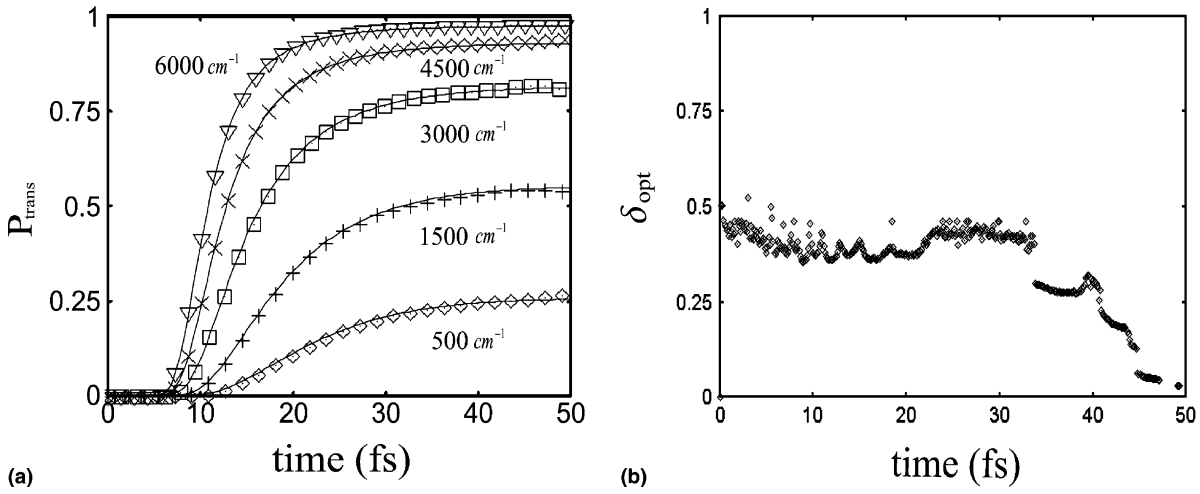

Fig. 6. Plot (a) displays the QTM/RBF results for the transmission probability as a function of time for five wave packets of different energies traveling on an uphill ramp potential. The solid line was calculated from a finite difference, fixed-grid method. Plot (b) shows the time-dependence of the multi-quadric shape parameter for the wave packet with an energy of 1500 cm^{-1}.

When the uphill potential was studied with a *constant* shape parameter, it was found that with $\delta = 0.26$ the simulation survived for approximately the same number of time steps as the time-dependent parameter study. In this case, once again, using a time-dependent algorithm would not be necessary and would only increase the time taken for the simulation while having little effect on the accuracy of the solution. This may not be the case, however, for all uphill potentials, since interference affects are amplified as the ramp becomes steeper. To find a model where it is necessary to utilize a time-dependent algorithm, it seems that a more complicated potential should be introduced.

5.3. Model 3: the downhill ramp/harmonic oscillator

The last model studied was the propagation of an initial 2D Gaussian wave packet under the external potential

$$V(x,y) = \frac{V_1}{1+\mathrm{e}^{-2.5(x-1)}} + \frac{1}{2}V_2 y^2\left(\frac{2}{1+\mathrm{e}^{2.5(x-1)}} + \frac{1}{1+\mathrm{e}^{-2.5(x-1)}}\right), \tag{27}$$

with $V_1 < 0$ and $V_2 > 0$ (see Fig. 7). Such a potential, for example, may represent a molecule's vibrational relaxation during an exothermic reaction. Because of the (x,y) coordinate coupling, this particular potential energy surface does not allow for a separable solution of the Schrödinger equation, thus presenting an even more complicated and interesting problem than that of the first two models. Table 6 displays the initial conditions used in the simulation.

Fig. 8 shows the time-development of the initial Gaussian wave packet in the harmonic oscillator/downhill ramp potential. Because most of the errors associated with the simulation accumulate at the

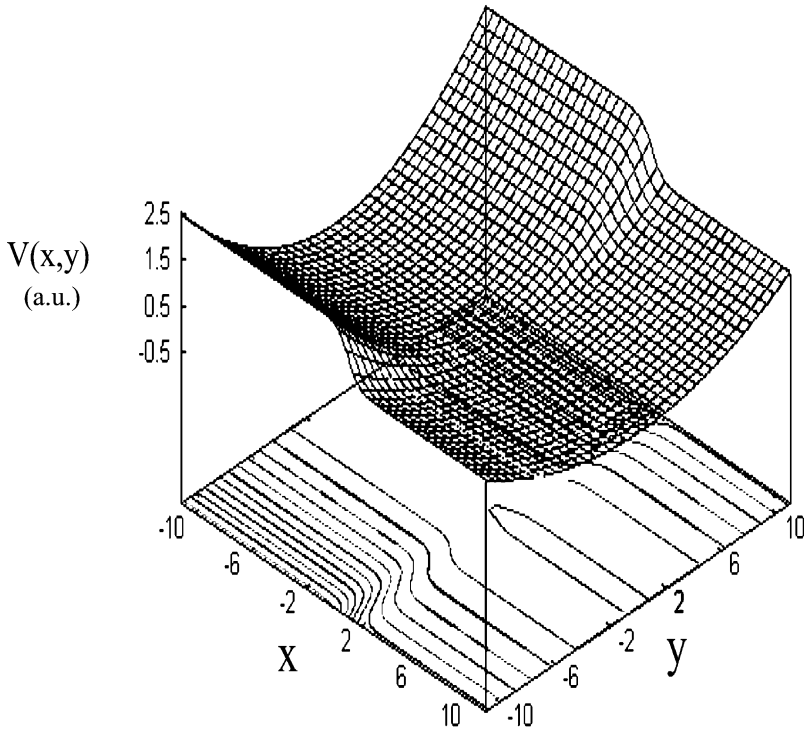

Fig. 7. A mesh–contour plot of the downhill ramp/harmonic oscillator potential used in model 3. All units are in a.u.

Table 6
2D wave packet parameters for the downhill ramp/harmonic oscillator

β_x	8
β_y	8
Energy	1500 cm^{-1}
m	2000
(x_0, y_0)	(0,0)
v_{x0}	0.0068
v_{y0}	0
Δx	0.075
Δy	0.075
np	17×17 grid, $np = 289$
dt	0.5

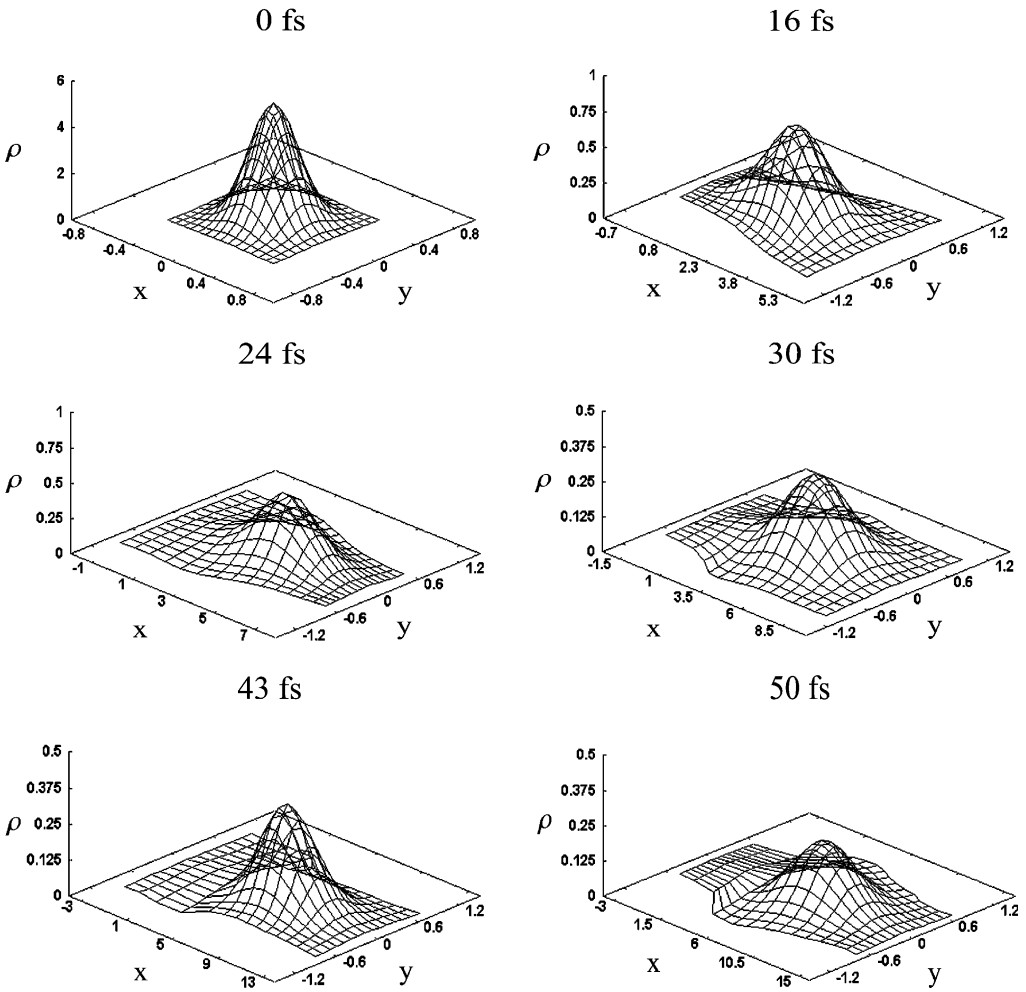

Fig. 8. Time-evolution of the density, ρ, for an initial Gaussian wave packet under the influence of the harmonic oscillator/downhill ramp potential described in model 3.

boundaries, only the inner 225 of the 289 fluid elements were plotted in this figure. The effect of the vibrational relaxation for those fluid elements that are transmitted becomes evident in the asymmetry of the grid as it is propagated in time. The wave packet was propagated for 50 fs, with computational break down occurring shortly thereafter.

Lastly, Fig. 9 shows how the optimum MQ shape parameter changes with time. Although there is the same decay in the δ parameter as with the uphill ramp, the trend has a slightly more complicated form. In this model, the decay begins at $t = 0$ and continues until approximately 15 fs, where there is a rise and subsequent oscillation in the shape parameter for about 10 fs, until the decay occurs again. The effect of this complicated trend of the shape parameter on the survival time of the simulation can be seen in Fig. 10. In this figure, independent trial simulations were conducted on the harmonic oscillator/downhill ramp potential energy surface using 23 different *constant* shape parameters ranging from 0.1 to 0.54. Each simulation was allowed to run until computational breakdown occurred. The number of time steps taken before breakdown for each of the constant MQ shape parameters is plotted in this figure. The longest constant parameter trial simulation proceeded for 2873 time steps, or 34.76 fs. When the same simulation was conducted with the δ optimizing algorithm, the simulation survived for 4389 time steps, a remarkable 53% increase in the survival time of the simulation. Because of these results, it is apparent that for this particular model, a time-dependent MQ shape parameter is needed for more accurate interpolations as the amplitude and phase progress in time. An explanation of this could be that the initial Gaussian wave packet, evolved under the harmonic oscillator/downhill ramp potential energy surface, suffers more amplitude or phase distortion than that of models 1 and 2. Because the optimum shape parameter depends on the form of the function to be interpolated, this distortion may change the optimum δ in time such that any constant parameter will not perform as well as a time-dependent shape parameter, which can adapt to the function deformation. Also, as can be seen from Fig. 8, the Lagrangian grid structure established in time by the moving fluid elements becomes very irregular due to the (x, y) coupling not seen in the first few models of this study. Because of this evolving grid structure, the conditioning of the coefficient matrix may change with time, resulting in a significant difference between the chosen optimal shape parameters as time moves on. A time-dependent δ choosing algorithm alleviates this problem, since it can adapt to not only the

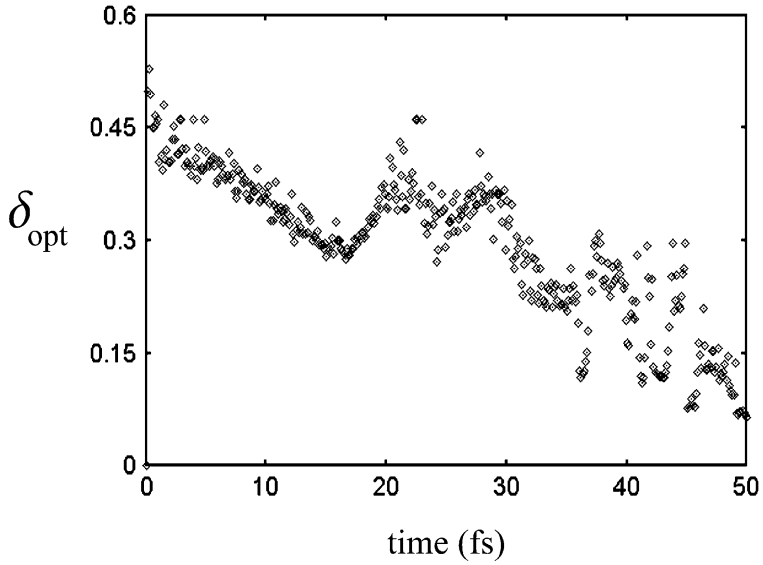

Fig. 9. Time-dependence of the multi-quadric shape parameter for model 3.

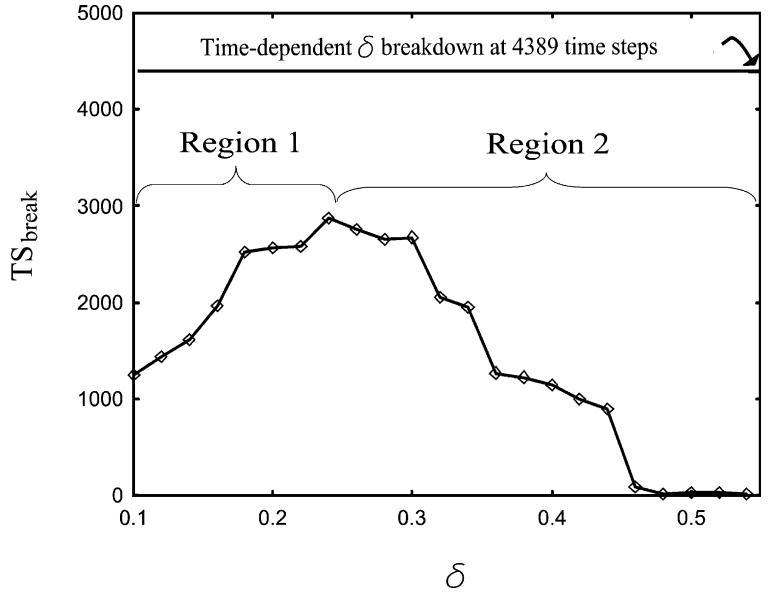

Fig. 10. The number of time steps taken before computational breakdown (TS_{break}) of model 3 while using a constant MQ shape parameter. The largest number of time steps propagated, 2873, was with a constant shape parameter of 0.24. By using a time-dependent shape parameter, the number of time steps before breakdown was increased by approximately 53%.

form of the function to be interpolated, but also to the grid structure defined by the current fluid element arrangement.

6. Conclusion

In conclusion of this study, a few statements must be made concerning the results of Section 5 and the practical use of free-parameter radial basis function interpolation in the quantum trajectory method. It should be reemphasized that a good RBF shape parameter represents the best possible compromise between the inherent ill-conditioning of the RBF coefficient matrix and the smoothest possible interpolate. Prior to this study, radial basis function interpolation in quantum hydrodynamics has been performed with time-constant shape parameters [24,25]. While this strategy may work quite well for some quantum mechanical problems, this may not be the case for more complicated potentials such as the one used in model 3 of this study. It was shown that in certain models, especially those in which the function to be interpolated is greatly distorted from its original form, a time-dependent shape parameter can dramatically increase the survival time of the computation. The cost of finding a new parameter at each time step, however, can become time consuming, and depending on the algorithm for finding the parameter, maybe unreasonable. Rippa's technique [43] for obtaining a good shape parameter was at least nine times slower than a constant parameter RBF interpolation. In a 2D simulation with few grid points, this was an acceptable sacrifice for the increase in survival time; however, it may not be reasonable for 3D or higher-dimensional models. In such cases where time cannot be sacrificed, a suitable shape parameter algorithm can be implemented initially and then periodically recalled throughout the simulation instead of at every time step.

Lastly, although optimized RBF interpolation has provided reasonable results for the simple QTM problems discussed in this study, it should be emphasized that it does not completely solve the computational problems associated with the Lagrangian QTM. As time progressed, some grid regions were

under-sampled while others were over-sampled, leading to poor derivative estimates. One way to remedy this problem is to use more fluid elements; however, the number of fluid elements was limited by the conditioning of the RBF coefficient matrix. Because of this, some models attempted such as the transmission of a wave packet through an Eckart barrier, were not as successful. Ideally, a relatively high-resolution grid is needed for such a model since interference effects result in oscillations in the reflected amplitude that are difficult to interpolate on an under-sampled mesh. Also, to properly utilize larger grids in radial basis function interpolation, domain decomposition must be incorporated into the algorithm to reduce the size of the coefficient matrix. In the future, higher resolution Lagrangian meshes will be further studied with optimized radial basis function interpolation so that more complicated potentials, such as the Eckart barrier, can be solved.

Acknowledgements

The authors thank Kyungsun Na, Keith Hughes, and Fernando Sales Mayor for useful discussions and editing. We also thank S. Rippa for help with the computational details of his algorithm and the Texas Advanced Computing Center at the University of Texas for the use of the Cray SV1, Aurora. This research was supported by the Robert Welch Foundation and the National Science Foundation.

References

[1] E. Bittner, Quantum tunneling dynamics using hydrodynamic trajectories, J. Chem. Phys. 112 (2000) 9703.
[2] E.R. Bittner, R.E. Wyatt, Integrating the quantum Hamilton–Jacobi equations by wave-front expansion and phase space analysis, J. Chem. Phys. 113 (2000) 8888.
[3] D. Bohm, A suggested interpretation of the quantum theory in terms of "hidden" variables I, Phys. Rev. 85 (1952) 166.
[4] D. Bohm, A suggested interpretation of the quantum theory in terms of "hidden" variables II, Phys. Rev. 85 (1952) 180.
[5] D. Bohm, B.J. Hiley, The Undivided Universe: An Ontological Interpretation of Quantum Theory, Routledge, London/New York, 1993.
[6] L. de Broglie, C. R. Acad. Sci. Paris 183 (1926) 447.
[7] R.G. Brook, P.E. Oppenheimer, et al., Solving the hydrodynamic formulation of quantum mechanics: a parallel MLS method, Int. J. Quantum Chem. 85 (2001) 263.
[8] M.D. Buhmann, A new class of radial basis functions with compact support, Math. Comput. 70 (2001) 307.
[9] R.E. Carlson, B.K. Natarajan, Sparse approximate multiquadric interpolation, Comput. Math. Appl. 27 (1994) 99.
[10] R.E. Carlson, T.A. Foley, Interpolation of track data with radial basis methods: advances in the theory and applications of radial basis functions, Comput. Math. Appl. 24 (1992) 27.
[11] R.E. Carlson, T.A. Foley, The parameter R^2 in multiquadric interpolations, Comput. Math. Appl. 21 (1991) 29.
[12] V. Cherkassky, F. Mulier, in: Learning from Data: Concepts, Theory, and Methods, John Wiley, New York, 1998, p. 78.
[13] T.A. Foley, Near optimal parameter selection of multiquadric interpolation, J. Appl. Sci. Comput. 1 (1991) 54.
[14] R. Franke, Scattered data interpolation: tests of some methods, Math. Comput. 48 (1982) 181.
[15] M.A. Goldberg, C.S. Chen, S.R. Karur, Improved multiquadric approximation for partial differential equation, Eng. Anal. Bound. Elem. 18 (1996) 9.
[16] R.L. Hardy, Hardy's multiquadric-biharmonic method for gravity field predictions II, Comput. Math. Appl. 41 (2001) 1043.
[17] R.L. Hardy, A contribution of the multiquadric method: interpolation of potential inside the Earth: advances in the theory and applications of radial basis functions, Comput. Math. Appl. 24 (1992) 81.
[18] R.L. Hardy, Comments of the discovery and evolution of the multiquadric method: advances in the theory and applications of radial basis functions, Comput. Math. Appl. 24 (1992) xi.
[19] R.L. Hardy, Theory and applications of the multiquadric-biharmonic method: 20 years of discovery 1968–1988, Comput. Math. Appl. 19 (1990) 163.
[20] R.L. Hardy, Multiquadric equations of topography and other irregular surfaces, J. Geophys. Res. 176 (1971) 1905.
[21] T. Hastie, R. Tibshirani, J. Friedman, The Elements of Statistical Learning: Data Mining, Inference, and Prediction, Springer, New York, 2001.
[22] W. Haussmann, K. Jetter, M. Reimer (Eds.), Recent Progress in Multivariate Approximation. Proceedings of the 4th International Conference on Multivariate Approximation held at the University of Dortmund, Birkhäuser Verlag, Basel, 2001.

[23] P.R. Holland, The Quantum Theory of Motion: An Account of the de Broglie–Bohm Causal Interpretation of Quantum Mechanics, Cambridge University Press, New York, 1993.
[24] X. Hu, T. Ho, H. Rabitz, Solution of the quantum fluid dynamical equations with radial basis function interpolation, Phys. Rev. E 61 (2000) 5967.
[25] X. Hu, T. Ho, H. Rabitz, A. Askar, Multivariate radial basis interpolation for solving quantum fluid dynamical equations: radial basis functions and partial differential equations, Comput. Math. Appl. 43 (2002) 525.
[26] E.J. Kansa, A scattered data approximation scheme with applications to computational fluid-dynamics – I, Comput. Math. Appl. 19 (1990) 127.
[27] E.J. Kansa, A scattered data approximation scheme with applications to computational fluid-dynamics – II, Comput. Math. Appl. 19 (1990) 147.
[28] E.J. Kansa, Local, point-wise rotational transformations of the conservation equations into stream-wise coordinates: radial basis functions and partial differential equations, Comput. Math. Appl. 43 (2002) 501.
[29] E.J. Kansa, R.E. Carlson, Improved accuracy of multiquadric interpolation using variable shape parameters, Comput. Math. Appl. 24 (1992) 99.
[30] E.J. Kansa, Y.C. Hon, Circumventing the Ill-conditioning problem with multiquadric radial basis functions: application to elliptical partial differential equations, Comput. Math. Appl. 39 (2000) 123.
[31] C. Lopreore, R.E. Wyatt, Quantum wave packet dynamics with trajectories; reflections on a downhill ramp potential, Chem. Phys. Lett. 325 (2000) 73.
[32] C. Lopreore, R.E. Wyatt, Quantum wave packet dynamics with trajectories, Phys. Rev. Lett. 82 (1999) 5190.
[33] C. Lopreore, R.E. Wyatt, Electronic transitions with quantum trajectories I, J. Chem. Phys. 114 (2001) 5113.
[34] C. Lopreore, R.E. Wyatt, Electronic transitions with quantum trajectories II, J. Chem. Phys. 116 (2001) 1228.
[35] J.B. Maddox, E.R. Bittner, Quantum relaxation dynamics using Bohmian trajectories, J. Chem. Phys. 115 (2001) 6309.
[36] E. Madelung, Z. Phys. 40 (1926) 322.
[37] W.R. Madych, Miscellaneous error bounds for multiquadric and related interpolators: advances in the theory and applications of radial basis functions, Comput. Math. Appl. 24 (1992) 121.
[38] W.R. Madych, S.A. Nelson, Multivariate interpolation and conditionally positive definite functions II, Math. Comput. 54 (1990) 211.
[39] W.R. Madych, S.A. Nelson, Bounds on multivariate polynomials and exponential error estimates for multiquadric interpolation, J. Approx. Theory 70 (1992) 94.
[40] C.A. Micchelli, Interpolation of scattering data: distance matrices and conditionally positive definite functions, Constr. Approx. 2 (1986) 11.
[41] N.J.D. Powell, A Review of Methods for Multivariable Interpolation at Scattered Data Points: The State of the Art in Numerical Analysis, Oxford University Press, New York, 1997.
[42] W.H. Press, B.P. Flannery, S.A. Teukolsky, W.T. Vetterling, Numerical Recipes; The Art of Scientific Computing, Cambridge University Press, New York, 1986.
[43] S. Rippa, An algorithm for selecting a good value for the parameter c in radial basis function interpolation, Adv. Comput. Math. 11 (1999) 193.
[44] F. Sales Mayor, A. Askar, H.A. Rabitz, Quantum fluid dynamics in the Lagrangian representation and applications to photodissociation problems, J. Chem. Phys. 111 (1999) 2423.
[45] R. Schaback, A unified theory of radial basis functions: native Hilbert spaces for radial basis functions II. Numerical analysis in the 20th century, vol. I, Approximation theory, J. Comput. Appl. Math. 121 (2000) 165.
[46] R. Schaback, Holgar Wendland, Adaptive greedy techniques for approximate solution of large RBF systems, Numer. Algorithms 24 (2000) 239.
[47] R. Schaback, Improved error bounds for scattered data interpolation by radial basis functions, Math. Comput. 68 (1999) 201.
[48] R. Schaback, Approximation by radial basis functions with finitely many centers, Constr. Approx. 12 (1996) 331.
[49] R. Schaback, in: Creating Surfaces from Scattered Data using Radial Basis Functions. Mathematical Methods for Curves and Surfaces, Vanderbilt University Press, Tennessee, 1995, p. 477.
[50] R. Schaback, Error estimates and condition numbers for radial basis function interpolation, Adv. Comput. Math. 3 (1995) 251.
[51] R. Schaback, Lower bounds for norms of inverses of interpolation matrices for radial basis functions, J. Approx. Theory 79 (1994) 287.
[52] R. Schaback, Native Hilbert Spaces for Radial Basis Functions. I. New Developments in Approximation Theory, Birkhäuser, Basel, 1999.
[53] R. Schaback, A unified theory of radial basis functions: native Hilbert spaces for radial basis functions. II. Numerical analysis in the 20th century, vol. I, Approximation theory, J. Comput. Appl. Math. 121 (2000) 165.
[54] A.E. Tarwater, A parameter study of Hardy's multiquadric method for scattered data interpolation, UCRL-54670, 1985.
[55] Z. Wu, in: Solving Differential Equations with Radial Basis Functions. Advances in Computational Mathematics, Dekker, New York, 1999, p. 537.

[56] R.E. Wyatt, K. Na, Quantum trajectory analysis of multimode subsystem-bath dynamics, Phys. Rev. E 65 (2001) 016702-1.
[57] R.E. Wyatt, E. Bittner, Quantum wave packet dynamics with trajectories: implementation with adaptive Lagrangian grids, J. Chem. Phys. 113 (2000) 8898.
[58] R.E. Wyatt, D.J. Kouri, D.K. Hoffman, Quantum wave packet dynamics with trajectories: implementation with distributed approximating functionals, J. Chem. Phys. 112 (2000) 10730.
[59] R.E. Wyatt, Quantum wave-packet dynamics with trajectories: wave function synthesis along quantum paths, Chem. Phys. Lett. 313 (1999) 189.
[60] R.E. Wyatt, Quantum wave packet dynamics with trajectories: application to reactive scattering, J. Chem. Phys. 111 (1999) 4406.
[61] M. Zerroukat, A boundary element scheme for diffusion problems using compactly supported radial basis functions, Eng. Anal. Bound. Elem. 23 (1999) 201.
[62] X. Zhang, K.Z. Song, M.W. Lu, X. Liu, Meshless methods based on collocation with radial basis functions, Comput. Mech. 26 (2000) 333.